Journal Name

ARTICLE TYPE

Cite this: DOI: 10.1039/xxxxxxxxxx

On The Lubricity of Transition Metal Dichalcogenides: an *ab initio* Study†

Benjamin J. Irving,*[a] Paolo Nicolini[a] and Tomas Polcar[b]

Received Date
Accepted Date

DOI: 10.1039/xxxxxxxxxx

www.rsc.org/journalname

Owing to specific characteristics engendered by their lamellar structures, transition metal dichalcogenides are posited as being some of the best dry lubricants available. Herein, we report a density functional investigation into the sliding properties and associated phenomena of these materials. Calculated potential energy and charge transfer profiles are used to highlight the dependence of shear strength on chemical composition and bilayer orientation (sliding direction). Furthermore, our calculations underscore the intrinsic relationship between incommensurate crystals and the oft-touted *superlubric* behaviour of molybdenum disulfide.

1 Introduction

Friction is defined as a *force that resists the sliding or rolling of one solid object over another*.[1] It is generally regarded as an adverse phenomenon, as it is a retarding force that continuously opposes the desired action of mechanical components. Reduced friction between mechanical parts in contact diminishes energy consumption, vibrations, noise, contact temperature, and wear. Although the inimical effects of friction and wear are perhaps most obvious in the macroworld, curtailing these effects in the nanoworld is an increasingly important challenge. Indeed, friction is a key obstacle to the miniaturisation of devices such as the read/write head in a hard drive:[2] due to their high surface-area-to-volume ratio, nanoscale components are particularly prone to degradation by friction and wear under tribological conditions. This problem has spurred on research on *superlubricity*, a (near) frictionless regime where two crystalline surfaces slide over one another in dry, incommensurate contact.

Generally speaking, in order to reduce friction between surfaces in contact, we must reduce the adhesive forces that exist between the microscopically irregular contact regions known as *asperities*. This is typically achieved by introducing an oil- or water-based lubricant to the interfacial region. To circumvent any potential shortcomings associated with wet lubrication (risk of contamination, failure to perform under extreme conditions *etc*) engineers are beginning to exploit solid state lubricants such as graphene[3,4] boron nitride,[5–7] and transition metal dichalcogenides (TMDs).[8–16] Solid lubricants proffer a number of advantages over wet lubricants, such as low evaporation rate, increased working temperature range and corrosion resistance.[17,18]

TMDs, of general form MX_2 ($M = Mo, W$; $X = S, Se, Te$), are a family of materials that display exploitable properties such as variable electronic behaviour and diverse phase transitions as a function of external parameters.[19] The unique properties of TMDs render them suitable for use in a wide range of technologies including nano-/opto-electronics,[20–27] catalysis,[28–31] and of course as solid lubricants.[8–13] TMDs exist in two crystal forms: hexagonal and rhombohedral. The hexagonal 2H polytype is both the most common and important for tribological applications, and so the calculations presented herein will focus on this polytype. The rhombohedral 3R form is also found in nature, albeit less commonly than 2H, as well as in synthetic materials. Both polytypes comprise the same $X-M-X$ layers stacked atop one another, although the orientation of the adjacent layers is parallel in 3R and anti-parallel in the 2H polytype. Of course, this difference in stacking arrangement splits the degeneracy between 2H and 3R. The effects of bilayer orientation on the sliding motion of MoS_2 have been thoroughly studied by Levita *et al*.[32,33] In particular, they demonstrated the importance of electrostatic interactions (which become increasingly significant with increasing load) for antiparallel layers, which may have important consequences for the fabrication of ultralow friction devices.

The hexagonal form exhibits six-fold symmetry, two MX_2 moieties per unit cell, and a lamellar structure, as shown in Fig 1. Each chalcogen atom is equidistant from three transition metal atoms, and each transition metal atom is equidistant from six chalcogen atoms.[34] There is a strong covalent bonding interaction between Mo and S, but the lattice layers are only held to-

[a] *Department of Control Engineering, Faculty of Electrical Engineering, Czech Technical University in Prague, Karlovo Náměstí 13, 121 35 Prague, Czech Republic; E-mail: irvinben@fel.cvut.cz*

[b] *National Centre for Advanced Tribology (nCATS), Faculty of Engineering and the Environment, University of Southampton, SO17 1BJ Southampton, United Kingdom*

† Electronic Supplementary Information (ESI) available: [details of any supplementary information available should be included here]. See DOI: 10.1039/b000000x/

gether by weak van der Waals (vdW) forces. These characteristics in particular render TMDs suitable for use as low friction coatings: whilst adhesive forces between MoS_2 and solid substrates are usually strong, the cohesive forces between lamellae of MoS_2 are low. The upshot of this is that the coefficient of friction between lamellae will be markedly lower that that between a lamella and the substrate, therefore, slip will occur preferentially between lamellae.

For sputtered MoS_2 coatings under ultrahigh vacuum it has been demonstrated that during sliding the vanishing of the friction force may be due to frictional anisotropy in the interface between domains in rotational disorder, *i.e.*, intercrystallite slippage of rotated S-rich hexagonal lattices.[35] Martin *et al*[36] also demonstrated the association between low friction coefficient (*ca.* 10^{-3} range) and friction induced 'easy-shear' basal planes of the MoS_2 crystal structure parallel to the sliding direction. Moreover, an orientation disorder around the *c*-axis was observed, indicating that frictional anisotropy during intercrystallite slip is likely to be the origin of the vanishing friction force. From a theoretical perspective, in order to rationalise the interplay between incommensurability and sliding energetics, Blumberg *et al*[37] utilised the *registry index* concept,[38,39] which is an efficient tool for quantifying registry mismatch in bilayer systems. They found a direct relation between the sliding potential energy surface and the interlayer registry, highlighting the most important geometrical features of the MoS_2 layers in determining the sliding physics under different tribological scenarios. Onodera *et al*[40] adopted a molecular dynamics method for studying the dynamical friction of two-layered MoS_2. Rotational disorder was imparted to the bilayer system by rotating the top layer from 0° to 60° (both commensurate) in 5° intervals. During the friction simulation, the incommensurate structures yielded low friction as a result of cancellation of the atomic force in the sliding direction, producing smooth motion. Conversely, for the commensurate systems, the S atoms at the interface are sliding over one another simultaneously whilst atomic forces are acting in the same direction, effectively producing a hundredfold increase in the calculated friction force.

A useful analogy for gaining insight into the 'friction-vs-commensurability' relationship is that of two 'egg-box' sheets in contact with one another. If the egg boxes are stacked in a commensurate fashion and we try to shear them, the unit cells all have to cross the same physical barriers simultaneously. In turn, the result is high static friction and stick-slip behaviour, resulting in high dynamical friction.[41] However, if the egg boxes are rotated relative to one another, yielding an incommensurate state, all unit cells now only have to cross a much smaller barrier at any point along the sliding path, *i.e.*, we expect reduced resistance towards shear/sliding. Whereas we are overcoming obvious physical barriers when sliding egg boxes over one another, for (atomically smooth) lamellar materials the energetic barriers are caused by enhanced Pauli repulsions between the overlapping electron clouds as they encounter each other during the sliding process.[42–45]

The aim of this paper is twofold. Firstly, we have performed a study similar to that reported by Levita *et al*,[32] but enlarging it to include the whole TMD family (*i.e.*, compounds with general formula MX_2, with $M = Mo, W$ and $X = S, Se, Te$). For each compound we calculated the potential energy surface (PES), enabling the estimation of the maximum static force that is necessary to be applied to a layer in order to observe sliding. The detailed analysis of the fundamental atomic interactions allowed us to systematically highlight the effect of the stoichiometry on the intrinsic frictional behaviour of the different materials. Additionally, in order to increase the predictive power of the presented results, we also provide a way to rationalise the findings, along with correlating the intrinsic tribological performance of the materials with simple physico-chemical properties such as electronegativity.

Secondly, the results represent further progress toward the understanding of superlubric features and their relation to layer orientation. The synergy between crystalline misfit angles and (super)lubric performance is fairly well reported on, particularly in the experimental literature, but a fully *ab initio* description of the interplay between interfacial (in)commensurability and frictional properties is currently lacking for TMDs. By exploiting accidental angular commensuration[43,46] we calculated potential energy landscapes (and, from these, maximal shear strengths) of bilayer MoS_2 for three different misfit angles. This allowed us to correlate the improved frictional properties of incommensurate configurations to the change in the atomic contributions to the overall layer interaction. The simulations presented herein not only improve our understanding of the (super)lubric behaviour of TMDs, but they also represent a key advancement in the 'bottom-up' approach to the design of tribological materials, as we are able to rationalise the sliding behaviour of TMDs using only fundamental quantum chemical parameters.

2 Methods

Periodic density functional theory (DFT) calculations have been performed using the *Vienna Ab-initio Simulation Package* (VASP).[47–50] Calculations were performed using projector-augmented wave pseudopotentials[51,52] and the Perdew-Burke-Ernzerhof functional,[53] with vdW interactions accounted for using the DFT-D2 method of Grimme;[54] this methodology has been demonstrated as being robust and reliable, accurately reproducing fundamental structural features.[55] Brillouin zone integrations utilised k-point grids generated automatically using the Monkhorst-Pack scheme:[56] a 15×15×15 grid was used for (bulk, 2H phase) unit cell optimisations, which was subsequently reduced to a 15×15×1 grid for the homogeneous MX_2 bilayers. Owing to the significant increase in the size of the unit cell of the incommensurate* bilayers, a 7×7×1 grid was employed for angles of 38.2 (Mo×14; S×28) and 92.2 (Mo×26; S×52) degrees, and a 5×5×1 grid for an angle of 17.9 degrees (Mo×62; S×124), in order to render them computationally tractable.

In concurrence with previous density functional calculations,[32,33] generating the sliding potential energy profile entails calculating the potential energy as the origin of the upper MX_2

* Throughout the remainder of the text we use the term 'incommensurate' to refer to configurations that show a mismatch due to an arbitrary misfit angle between the layers

layer is shifted along the long-diagonal of the unit cell, corresponding to the [1100] direction, represented by distance '*y*' in Fig 2. Incommensurate bilayers were attained using accidental angular commensurations.[43,46] The space group of each bilayer was confirmed using the FINDSYM software[57,58] and symmetry operations checked using space group diagrams and tables.[59] Regarding the simulation setup of the incommensurate MoS_2 layers, owing to the larger distances traversed by the upper layer and the switch from a $P6_3/mmc$ to P312 space group, we doubled the number of points calculated in each potential energy profile, so as not to miss any structurally/energetically important bilayer configurations. In effect, step-sizes are now $1/24^{\text{th}}$ of the long diagonal 'y'. For all potential energy profile calculations, M atoms were frozen in the *xy*-plane, but free to move in *z*; all X atoms were fully relaxed.

3 Results & Discussion

All primitive cells were generated using diffraction data obtained via the *STFC Chemical Database Service*.[60] Following the optimisation of each MX_2 bulk cell, lattice parameters for which are reported in Table 1, transformation to a bilayer system was simply achieved by introducing a vacuum of at least 20 Å above the 'top' layer. Important nanomechanical properties of the TMD bilayers have also been calculated:

- **bilayer binding energy:** $\mathrm{E_{bind}} = \mathrm{E_{bilayer}} - (2 \times \mathrm{E_{monolayer}})$
- **interfacial adhesion energy:**† $\gamma = \mathrm{E_{bind}}/\mathrm{A}$
- **ideal shear strength:**‡ $\tau_y = \mathrm{f_{max}}/\mathrm{A}$

The calculation of an ideal interfacial shear strength is based on the findings of surface forces apparatus experiments[61] and atomic force microscopy studies[62,63] in which it is reasoned that, in the absence of wear, the frictional force (F_f) is directly proportional to the contact area, *i.e.*, $F_f = \tau A$, where τ is the shear strength. Given the primitive nature of the interfaces considered within this study, and the complete absence of *e.g.* tribochemical reactions, we can assume that a lower value for interfacial shear is a good indicator of a lower coefficient of friction.

Commensurate bilayers

Evaluating the potential energy profiles of TMDs during sliding helps rationalise the mechanisms that underlie the tribological properties of TMDs, revealing the stereoelectronic nature of the sliding interfaces.[32] Sliding profiles for the primitive MX_2 ($M = Mo, W$ and $X = S, Se, Te$) systems are shown in Figs 3 and 4. Also shown within Fig 3 are the three most important MoS_2 geometries, corresponding to the *global* minimum energy stacking arrangement (d*y* = 0.00 Å), a second *local* minimum (d*y* = 1.84 Å; $\frac{1}{3}$y) and the *global* potential energy maximum (d*y* = 3.68 Å; $\frac{2}{3}$y). Although rendered structures are only shown for MoS_2, the same general structure *vs.* energetics relationship is consistent for all bilayer stoichiometries considered herein. The starting (ending) configuration of each bilayer corresponds to the optimised minimum energy stacking motif,[64] in which the chalcogen atoms in the top layer sit directly above the M atoms in the bottom layer. As this represents the most energetically favourable configuration, we used this to set the zero-point for the energy. A local minimum for each system (d*y* = 1.84 Å or $\frac{1}{3}$y for MoS_2) is characterised by the chalcogens in one layer directly facing a 'hollow' site in the partner layer. All potential energy profiles also exhibit two energy maxima; these are attributable to stacking arrangements in which the X atoms (i) reside at an intermediate *bridging* position (d*y* = 0.92 Å or $\frac{1}{6}$y for MoS_2) or (ii) directly atop one another (d*y* = 3.68 Å or $\frac{2}{3}$y for MoS_2), where repulsion between chalcogen atom lone pairs is maximised.[32,33] Interlayer distances for the energetically important points along each profile are reported in Table 2. For all MX_2 systems, it can be seen that energy minima (maxima) correlate with reduced (increased) interlayer distances, as expected. In Table 3 we also report calculated nanomechanical properties (E_{bind}, γ and τ_y) that underpin bilayer shear behaviour. Values for MoS_2 are in good agreement with previous DFT results reported by Levita *et al.*[32,33]

Focusing on MoX_2 stoichiometries, the electronic contributions to the interlayer attraction (repulsion) at the global energy minimum (maximum) are evident in the charge density difference plots:§ presented in Fig 5 are the charge density difference isosurfaces for the global energy minimum and maximum of MoS_2, and the corresponding plane-averaged charge density profiles for all MoX_2 stoichiometries are shown in Fig 6. For extra clarity, individual charge density profiles for each TMD, showing atomic positions within the cell, can be found in the ESI. Further detailed analysis of the potential energy *vs.* charge density relationship is also provided in the ESI, in which we detail the changes in potential energy *vs.* the integral of charge density accumulation at the interface for each unique geometry.

Generally speaking, for charge density difference plots, positive (negative) values should correspond to an area of electron density enrichment (depletion). In corroboration of Levita *et al*,[32] these plots show that an energy minimum is generally coincident with extended charge accumulation at the center of the interface, whereas at energy maxima (chalcogens 'on top' of one another), the interface is depleted, with charge accumulation occurring only on the chalcogens. Comparing the profiles for the three energy minima, charge enrichment within the bilayer cavity is greatest for $MoTe_2$, which in conjunction with (greatest) charge depletion at Te, should yield the strongest interlayer binding interaction; this is supported by the calculated γ values in Table 3. For the three maxima, the profiles in Fig 6 exhibit similar trends. However, charge accumulation within the MoS_2 interlayer cavity is negligible in comparison with the Se and Te analogues, and

† A is unit cell cross-sectional area; γ is defined as the energy per unit area required to separate the layers from equilibrium to infinity

‡ $\mathrm{f_{max}}$ is the maximum lateral force experienced during sliding along 'y', i.e., steepest PES gradient: $\mathrm{f(y)} = \mathrm{dE/dy}$; τ_y is defined as the maximum load applied parallel to the face of the material that the material can resist prior to sliding

§ Charge density difference requires the total charge density of the optimised bilayer, ρ_{bilayer}, and the charge density for the individual components, *i.e.*, ρ_{top} and ρ_{bottom}. The difference may then be calculated as: $\Delta\rho = \rho_{\mathrm{bilayer}} - \rho_{\mathrm{top}} - \rho_{\mathrm{bottom}}$

so again we expect to calculate the weakest interlayer binding between the MoS_2 lamellae. Indeed, at the global energy maximum along each profile, we observe the same trend in E_{bind} values: MoS_2 (96.76 meV) < $MoSe_2$ (135.43 meV) < $MoTe_2$ (184.21 meV). By combining the outcomes for minima and maxima, and knowing that the shape of the profiles does not depend on the stoichiometry, it is reasonable to expect the highest (lowest) slip 'activation barrier' for $MoTe_2$ (MoS_2). This is in fact supported by the values reported in Table 3. Results in Table 3 also show that τ_y varies with the chalcogen as: S < Se < Te. In order to quantify the accumulation of charge between lamellae, we calculated the difference between minimum and maximum configurations in the integrals of the charge density peak in the interlayer region. As a confirmation of the qualitative reasoning drawn above, we found a monotonic dependence of the calculated shear strength values as a function of these integrals, as reported in Fig 7. Moreover, we also observe a correlation between the calculated γ values and both f_{max} and τ_y, which is not always evident in experiment,[63] that is, a greater interfacial adhesion energy may be indicative of greater resistance to interfacial shear. This behaviour can be explained in terms of the *Cobblestone Model*.[61,65–67] Briefly, it considers a rigid object moving over a rough surface in the presence of an attractive force between the two. To allow movement over the surface, the object has to overcome the barriers represented by the asperities. For an atomically smooth sample, the 'cobblestones' are considered representative of atomic corrugation.[63] To a first approximation, one can assume that E_{bind} is proportional to the adhesive work needed by the layer in traveling one lattice distance, *i.e.*, passing from one minimum to another *via* a maximum in the potential energy surface. In this case, it follows that adhesion and the maximum lateral force should increase in tandem. In turn, under these idealised conditions, the calculated properties point to MoS_2 as the better Mo-based lubricant considered in this study.

Returning to Fig 4, we report the calculated PES for each of the three W-based TMDs. The plane-averaged charge density profiles for the WX_2 series are presented in Fig 8; in order to highlight the effect(s) of changing both the transition metal and chalcogen atom, the charge density difference isosurface for WSe_2 is provided in the ESI, which can be compared to the MoS_2 profile in Fig 5. As is evident in their respective profiles, the stereoelectronic nature of the key geometries are near-identical for MoS_2 and WSe_2. There are only subtle quantitative differences in *e.g.* the charge borne by the transition metal or chalcogen atoms at the key geometries, but they are qualitatively near-identical. As with the Mo-based series, results reported in Table 2 confirm that energy minima (maxima) exhibit the smallest (largest) interlayer distances, owing to the reduced (enhanced) Coulombic repulsion between the layers, which is dependent on relative positions of the chalcogen atoms. As with the MoX_2 series, charge density distribution can be directly linked with interlayer binding energies. For the three global energy minima, E_{bind} again varies with chalcogen as S < Se < Te (values reported in Table 3), with the same trend in E_{bind} observed at each global energy maximum: WS_2 (177.51 meV) < WSe_2 (213.48 meV) < WTe_2 (258.61 meV). In unanimity with the Mo-based analogues, the calculated ideal shear strengths (Table 3) suggest that τ_y varies with the chalcogen as: S < Se < Te. Moreover, it is also possible to correlate τ_y with both the calculated γ values, as well as the integrals of the difference between the charge density peak in the interlayer region at minimum and maximum configurations.

As our simulations are considering perfectly flat MX_2 layers, *i.e.*, a complete absence of asperities/contaminants, with sliding conditions identical for each TMD, any differences between the potential energy profiles are caused wholly by the physical chemistry intrinsic to the system. Focusing on the charge distributions presented above, it is evident that all MX_2 compounds exhibit a small decrease in charge density on the metal between the global maximum and minimum configurations. Conversely, there is a more marked increase of charge density on the chalcogen between the two configurations. Given these observations, it is possible to speculate that a property as simple as the Pauling electronegativity (χ) can be used to rationalise the trends observed. For the transition metals considered in this study, we have χ values of $\chi_{Mo} = 2.16$ and $\chi_W = 2.36$; the chalcogens have χ values of $\chi_S = 2.58$, $\chi_{Se} = 2.55$ and $\chi_{Te} = 2.10$.[68,69] As slippage between planes is facilitated by the presence of enhanced (slightly decreased) charge accumulation on the chalcogens (metals), the 'ideal' metal-chalcogen combination will yield a TMD that allows for a greater proportion of the charge to be borne by the chalcogens. In order to achieve this state, we require some electron-donation from the transition metal (which will tally with a lower χ) and good electron-acceptor behaviour from the chalcogen (*i.e.*, higher χ). Upon inspection of the χ values it is evident that the ideal combination among the studied compounds would be Mo + S, whilst the least favourable combination is W + Te. By assuming that geometrical and electronic contributions are qualitatively comparable also in other lamellar TMDs, one may use χ values to predict the energetic barrier on the PES and ultimately the ideal shear stress τ_y. Of great intrigue to us is the prospect of exploring the actual effect on the PES profile upon replacement of the Mo atoms with some other less electronegative metal (for example, with Zr or Hf,[70], or with Ti[55]). In case it turns out that intrinsic frictional properties of TMD compounds can be effectively guessed from a property as simple as electronegativity, it will be a worthwhile effort to extend these studies and establish a deeper rationalisation of the correspondence, perhaps making use of approximated models.

Incommensurate MoS_2 bilayers

Having seen the effect of chemical changes on the lubricating properties of TMDs, we now consider the role of purely physical changes, namely *incommensuration*. Here we present a series of potential energy profiles pertaining to the sliding of mismatched MoS_2 bilayers. MoS_2 was selected for further investigation as not only do our calculations suggest this TMD has the best intrinsic frictional properties, but we must also improve our understanding of this fundamental aspect of MoS_2 lubrication. Indeed, with the development of increasingly sophisticated fabrication techniques that enable the user to control the deposition of TMDs on a substrate with preferred relative rotation angles,[71] developing a full

description of the angular dependence of frictional properties will only become an increasingly important facet of our knowledge.

In Fig 9 are top-down projections (along the z-axis) of the incommensurate bilayers. To serve as a reference, the first panel in Fig 10 is simply a reproduction of the MoS_2 potential energy profile from Fig 3. The second panel shows the sliding profile for bilayer MoS_2 with a lattice mismatch angle of 17.9°, which displays some very obvious differences to the commensurate scenario. The initial/final configurations and mid-point represent global and local energy maxima respectively, with all other intermediate geometries ca. 0.025 eV more stable than these configurations. Given that our periodic cell now contains 186 atoms (Mo $\times$ 62; S $\times$ 124), it is much harder to discern distinct structural features to which we can attribute this difference in energy. That said, it is again apparent that for each of the two energy maxima, there is a near-perfect eclipse of some pairs of S atoms in the bottom and top layer, thereby maximising Coulombic repulsion between the layers. All other intermediate geometries avoid such a scenario, although there will of course always be some 'partial eclipse' of S atoms throughout sliding. Throughout the entire profile, the average interlayer distance (calculated as the difference between average z-coordinate of Mo atoms in top layer and average z-coordinate of Mo atoms in the bottom layer) only changes by *ca.* 0.03 Å (in the range 6.50-6.53 Å), although somewhat counterintuitively the three maxima apparently have the smallest interlayer distance.

For a mismatch angle of 38.2°, the change in potential energy during sliding (third panel of Fig 10) exhibits a much more undulating profile. However, it is important to note that the alternations in energy in this instance are of order 1×10^{-4} eV, and so one does not expect to find any drastically different bilayer geometries from one point to the next. In this instance, we find that the average interlayer separation essentially remains constant throughout at 6.53 Å.

The potential energy profile calculated for an angle of 92.2°, as shown in the fourth panel of Fig 10, is essentially flat when compared with the commensurate system. Fluctuations in energy are now only of order 1×10^{-5} eV. Although each configuration is roughly isoenergetic, the changes in energy are within the tolerated error in total energy (1×10^{-6} eV) and so we can have confidence that the results are significant. As with the previous two mismatch angles, the lack of clearly defined bridge/hollow/eclipse geometries for incommensurate layers manifests itself in the flatness of the potential energy profile when compared to the commensurate case. As is the case for a rotation of 38.2°, the average interlayer separation remains constant for each step of the profile at 6.53 Å.

Reported in Table 4 are the important nanomechnical properties pertaining to each incommensurate setup, with results for commensurate MoS_2 repeated for ease of comparison. As expected, for each incommensurate angle, γ is lower than for the commensurate case. However, the most dramatic changes are apparent in the values calculated for f_{max} and τ_y. As the angle of incommensuration increases, each 'step' sees a reduction in f_{max} and τ_y of *ca.* one order of magnitude; that is, the greater the incommensurability, the easier it is to shear. To better understand what is happening during sliding of these incommensurate layers, we have plotted the plane-average charge density for MoS_2 with an incommensurate angle of 38.2° in Fig 11. The same plots for both the 17.9° and 92.2° case are provided in the ESI, and are unsurprisingly near identical to the profiles in Fig 11. As with the commensurate setup, we have chosen the global energy minimum and maximum as the key points of study. As is immediately obvious, there is no noticeable change in charge distribution, and so no change in the strength of the bilayer binding interaction is to be expected throughout the sliding process. Rather, we have a scenario in which there is constant repulsion between the lamellae, yielding exceptionally low values for the ideal shear strength, τ_y. The characteristics of these incommensurate layers is largely as expected, and has been explained above in general terms of the 'egg-box' model.

4 Conclusions

In this paper we report the results of extensive DFT calculations of several members of the TMD family (that is lamellar compounds of general formula MX_2, with $M = Mo, W$ and $X = S, Se, Te$). Specifically, for each compound, we have calculated the potential energy surfaces experienced by a layer that is rigidly sliding on top of another in a commensurate configuration. With this knowledge it is possible to define and estimate a simple descriptor (the ideal shear strength τ_y) for the intrinsic tribological properties of a material (of course, making rough assumptions such as the complete absence of asperities/contaminants). Moreover, from the analysis of the calculations, we described in detail the changes in the electronic density that occur during the sliding dynamics, finding that a qualitatively similar behaviour is shared by all the TMDs studied herein. This allowed us to formulate the conjecture that a simple atomic property such as electronegativity may be used to predict intrinsic tribological performance of other compounds of the TMD family.

In addition to this, we also made progress in developing our understanding of the superlubric behaviour observed in TMD-based systems. By exploiting accidental angular commensuration, we have been able to perform calculations on three different incommensurate configurations, giving an estimation of the roughness of the potential energy landscape with respect to the sliding coordinate. The results reveal that a decrease in friction of two to four orders of magnitude is expected when one moves from the commensurate configuration to an incommensurate one. This is particularly interesting if one considers that such a rotationally disordered configuration has recently been synthesised for WSe_2 *via* annealing of amorphous precursors, suggesting that progress is being made regarding fabrication of interfaces with non-random rotational angles.[72] Also for the incommensurate cases, we have conducted detailed analyses on the change of the electronic structure as consequence of sliding.

Future simulations will be used to improve our understanding of the frictional behaviour of TMDs by elucidating a number of closely related phenomena. Perhaps the most obvious extension of the work reported herein is to study more realistic surface topographies, as it has been shown[73] that contact surface roughness can directly influence the (static) friction coefficient. An-

other extension of the simulations presented here is to evaluate performance of the TMDs under varying sliding conditions, e.g. the effect(s) of load, temperature and sliding speed; this would likely require the combination of *ab initio* and classical molecular dynamics calculations, with the latter being used for the simulation of more realistic models and a wider range of conditions. Additionally, it is of paramount importance that we fully understand the role(s) of contaminants and dopants. For example, it is well known that the absence of contaminants is crucial to the low-friction properties of MoS_2, most notably water vapour either from ambient air or a humid environment; it has been suggested that liquid water can form *via* capillarity condensation in defects of MoS_2 crystals, subsequently affecting the easy shear between basal planes.[36] As such, it will be beneficial to fully understand the role of such contaminants, and even exploit computational methods in predicting contaminant species that may enhance the (super)lubricating properties of MoS_2.

Furthermore, as our results have highlighted the central importance of charge accumulation at the interface of the lamellae (*i.e.*, Coulombic repulsion), of particular interest is to study various defects that affect the electronic structure of lamellar TMDs in such a way that their presence enhances lubricant behaviour of various TMDs. For example, it is anticipated that if oxygen replaces even just a small fraction of sulfur atoms at the interface between two layers of MoS_2, the subsequent *reduction* in interlayer Coulombic repulsion will actually induce a high-friction state. Conversely, it has been predicted by our group that the presence of titanium (replacing Mo atoms) within MoS_2 may enhance the tribological performance of the material.[55]

By using this information to deepen our understanding of the synergy between interlayer interactions and frictional behaviour, we highlight the powerful **predictive** capabilities of *in silico* methods during the material design process. Indeed, it is the ultimate goal of any solid-state theoretician to be able to predict new materials with properties that surpass predecessors, without requiring input from experiment.[74]

5 Acknowledgements

The authors acknowledge the use of the Salomon HPC cluster administered by IT4Innovations National Supercomputing Center, University of Ostrava, Czech Republic; the IRIDIS High Performance Computing Facility, and associated support services at the University of Southampton; and the Abel Cluster, owned by the University of Oslo and the Norwegian metacenter for High Performance Computing (NOTUR), and operated by the Department for Research Computing at USIT, the University of Oslo IT-department, in the completion of this work. The use of VESTA is also acknowledged.[75] This publication was supported by the Czech Science Foundation, project 16-11516Y. The project 'Centre for Advanced Photovoltaics' was supported by Ministry of Education, Youth and Sport CZ.02.1.01/0.0/0.0/15_003/0000464. This work is partly supported by COST Action MP1303. The authors thank Dr Antonio Cammarata for his insightful contributions to this publication.

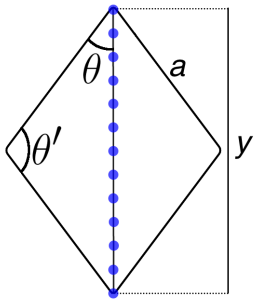

Fig. 2 Schematic of a generic **commensurate** MX_2 unit cell, with steps of $1/12^{\text{th}}$ of the long diagonal 'y' (the [1100] direction) represented by the blue dots. This step-size is chosen as these symmetry locations - as evident in the schematic of the $P6_3/mmc$ (No. 194) space group[59] - coincide with sampling the edges of the lattice irreducible zone.[32] Each datum calculated for a potential energy profile corresponds to the energy of a particular MX_2 bilayer configuration, whereby the origin of the top layer resides at a coordinate marked by a blue dot. The z-axis is out-of-plane, towards the reader.

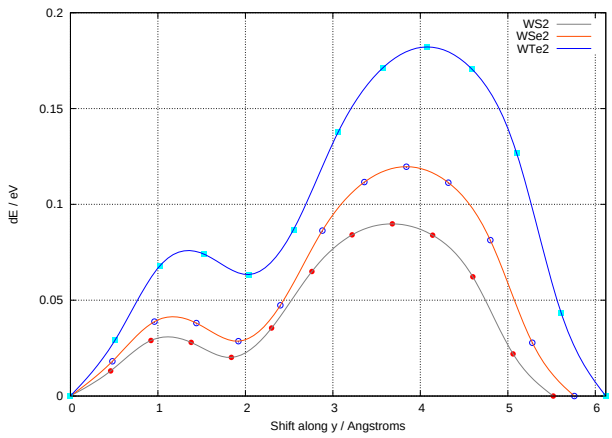

Fig. 4 Potential energy profiles (total change in energy per unit cell vs. shift along 'y') for the sliding of commensurate WX_2 bilayers (zero load, W atoms fixed in the xy-plane, X atoms free to relax).

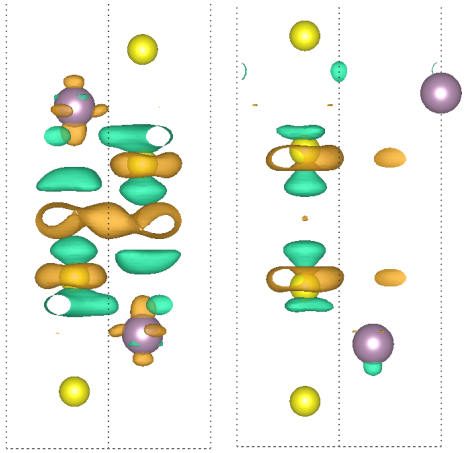

Fig. 5 Charge density difference isosurfaces (isolevel = 6.5×10^{-5} $e/\text{Å}^3$; positive = orange; negative = turquoise) for MoS_2 [L] at dy = 0.00 Å (global energy minimum) and [R] dy = 3.68 Å (global energy maximum).

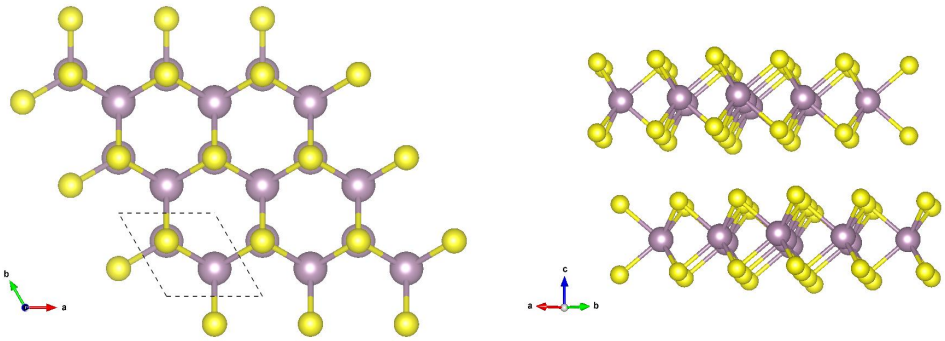

Fig. 1 [L] Top-down projection of the 2H phase of MoS_2; space group = $P6_3/mmc$ (No. 194), $a_{opt} = 3.192$ Å, $c_{opt} = 12.413$ Å; dashed line represents the unit cell employed for periodic calculations - here we show a 3x3 replica of the system [R] Side-on view of the same system, clearly showing the trigonal prismatic coordination of the molybdenum to each nearest neighbour sulfur atom.

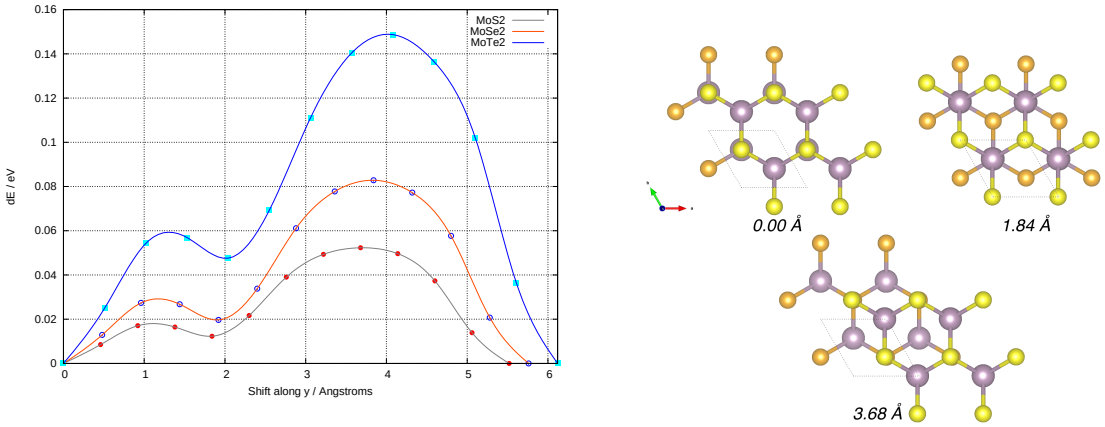

Fig. 3 [L] Potential energy profiles (total change in energy per unit cell vs. shift along 'y') for the sliding of commensurate MoX_2 bilayers (zero load, Mo atoms fixed in the xy-plane, X atoms free to relax) [R] Geometric arrangements of the most important positions along the PES profile of MoS_2 (Mo = purple; top layer S = yellow; bottom layer S = orange).

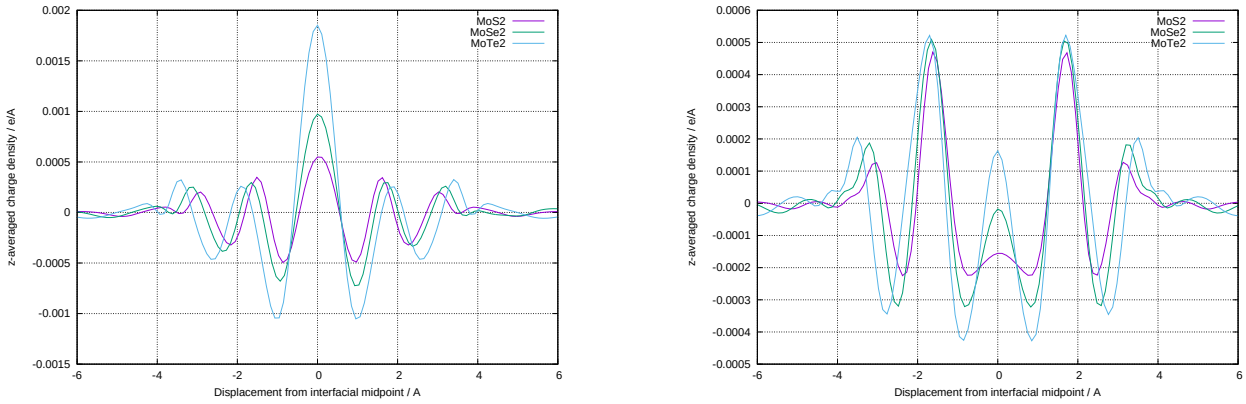

Fig. 6 Plane-average charge density for the commensurate MoX_2 bilayers, each at their respective global energy [L] minima [R] maxima.

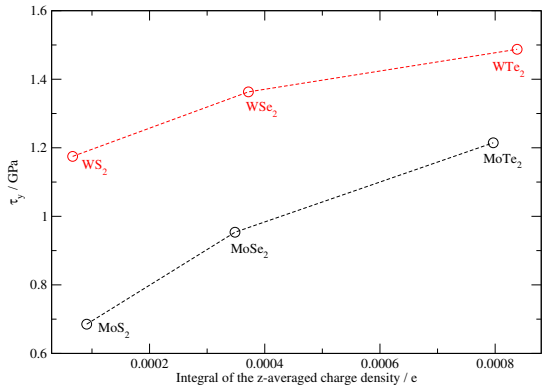

Fig. 7 Integrals of the difference in plane-average charge densities between the global energy minimum and maximum for all the studied compounds in the commensurate case. Dashed lines are guides for the eye.

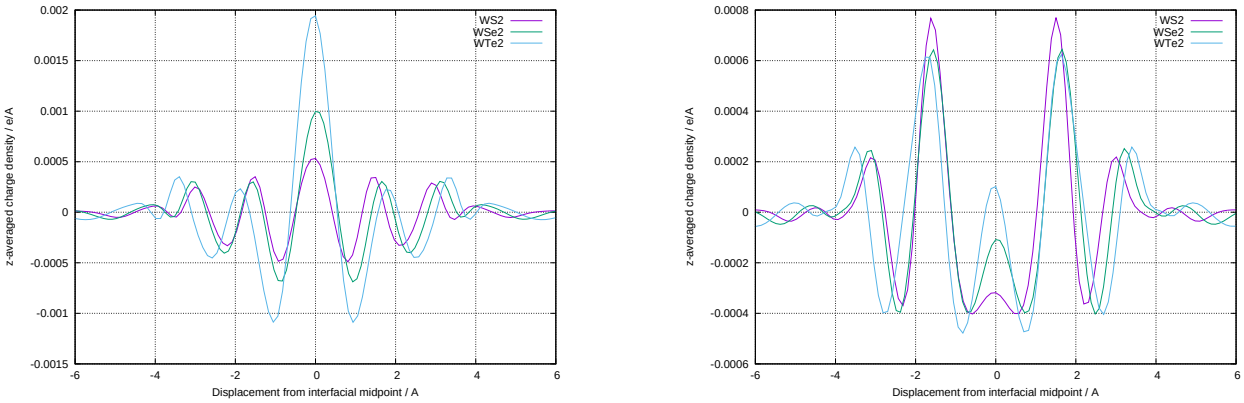

Fig. 8 Plane-average charge density for the commensurate WX_2 bilayers, each at their respective global energy [L] minima [R] maxima.

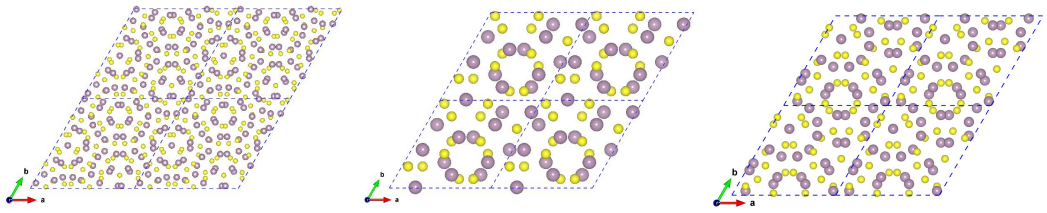

Fig. 9 Left to right: Renderings of 4x4 supercells for MoS_2 bilayers with incommensuration angles of 17.9°, 38.2° and 92.2°; space group = P312 (No. 149).

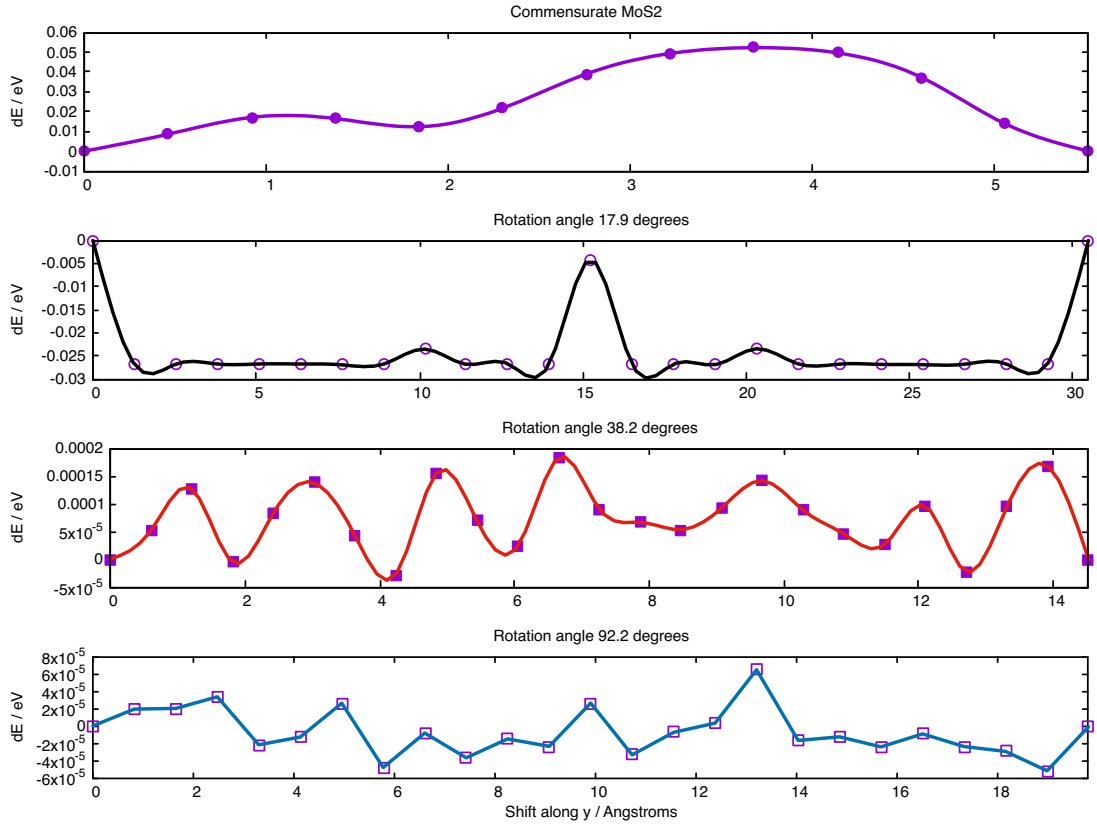

Fig. 10 Comparison of the potential energy profiles (total change in energy per unit cell vs. shift along 'y') for the sliding of commensurate MoS_2 and the three incommensurate analogues (zero load, Mo atoms fixed in the xy-plane, S atoms free to relax).

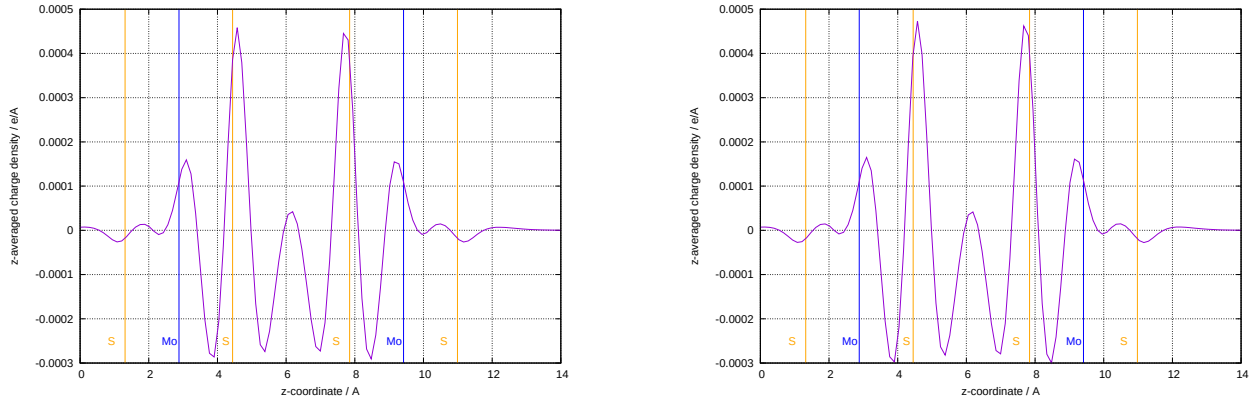

Fig. 11 Plane-average charge density for the MoS_2 bilayer system with the top layer roated 38.2 degrees relative to the bottom one at [L] dy = 0.00 Å (global energy minimum) and [R] dy = 6.655 Å (global energy maximum).

Table 1 Optimised unit cell parameters for each bulk TMD structure. The interlayer distance is defined as the vertical distance between the chalcogen atoms at the bilayer interface

TMD	a_{opt} / Å	c_{opt} / Å	Interlayer distance / Å
MoS_2	3.192	12.413	3.097
$MoSe_2$	3.321	13.058	3.198
$MoTe_2$	3.533	14.012	3.384
WS_2	3.178	12.419	3.074
WSe_2	3.321	13.119	3.212
WTe_2	3.523	14.440	3.562

Table 2 Variations in interlayer distance (vertical distance between chalcogen atoms at the bilayer interface, all values reported in Å) along the sliding potential energy profile for each commensurate MX_2 bilayer

System	$E_{min,global}$	$E_{max,local}$ ($\frac{1}{6}$y)	$E_{min,local}$ ($\frac{1}{3}$y)	$E_{max,global}$ ($\frac{2}{3}$y)
MoS_2	3.083	3.221	3.158	3.717
$MoSe_2$	3.188	3.329	3.239	3.759
$MoTe_2$	3.376	3.522	3.445	4.039
WS_2	3.001	3.079	3.030	3.543
WSe_2	3.089	3.214	3.137	3.667
WTe_2	3.290	3.464	3.421	3.967

Table 3 Nanomechanical properties calculated for each TMD bilayer

TMD	E_{bind} / meV (per cell)	γ/Jm^{-2}	f_{max} / eV/Å	τ_y/GPa
MoS_2	149.058	0.271	0.037738	0.6853
$MoSe_2$	218.230	0.366	0.056833	0.9536
$MoTe_2$	332.902	0.493	0.081934	1.2145
WS_2	267.337	0.490	0.064125	1.1748
WSe_2	333.132	0.559	0.081275	1.3631
WTe_2	440.756	0.657	0.099769	1.4874

Table 4 Nanomechanical properties calculated for each of the (in)commensurate MoS_2 bilayers

Angle of Rotation	E_{bind} / meV (per cell)	E_{bind} / meV (per MoS_2)	γ/Jm^{-2}	f_{max} / eV/Å	τ_y/GPa
0.00	149.058	74.529	0.271	0.037738	0.6853
17.9	3542.099	57.131	0.212	0.008902	0.0127
38.2	822.598	58.757	0.218	0.000105	0.0008
92.2	1530.061	58.849	0.218	0.000043	0.0001

References

1 *Britannica.com*, http://www.britannica.com/science/friction.

2 *Physics - Synopsis: Slip Sliding Away*, https://physics.aps.org/synopsis-for/10.1103/PhysRevLett.110.255504.

3 D. Berman, S. A. Deshmukh, S. K. R. S. Sankaranarayanan, A. Erdemir and A. V. Sumant, *Adv. Funct. Mater.*, 2014, **24**, 6640.

4 D. Berman, A. Erdemir and A. V. Sumant, *Mater. Today*, 2014, **17**, 31.

5 S. Watanabe, S. Miyake and M. Murakawa, *Surf. Coat. Technol.*, 1991, **49**, 406.

6 S. Miyake, S. Watanabe, M. Murakawa, R. Kaneko and T. Miyato, *Thin Solid Films*, 1992, **212**, 262.

7 J. M. Martin, Th. Le Mogne, C. Chassagnette and M. N. Gardos, *Tribol. T.*, 1992, **35**, 462.

8 M. Evaristo, T. Polcar and A. Cavaleiro, *Int. J. Mech. Mater. Des.*, 2008, **4**, 137.

9 T. Polcar, M. Evaristo, R. Colaço, C. Silviu Sandu and A. Cavaleiro, *Acta Mater.*, 2008, **56**, 5101.

10 J. V. Pimentel, T. Polcar and A. Cavaleiro, *Surf. Coat. Technol.*, 2011, **205**, 3274.

11 T. Polcar and A. Cavaleiro, *Thin Solid Films*, 2011, **519**, 4037.

12 T. Polcar and A. Cavaleiro, *Surf. Coat. Technol.*, 2011, **206**, 686.

13 A. A. Tedstone, D. J. Lewis and P. O'Brien, *Chem. Mater.*, 2016, **28**, 1965.

14 R. Lv, J. A. Robinson, R. E. Schaak, D. Sun, Y. Sun, T. E. Mallouk and M. Terrones, *Acc. Chem. Res.*, 2015, **48**, 56.

15 X. Hu, Torbjörkman, H. Lipsanen, L. Sun and A. V. Krasheninnikov, *J. Phys. Chem. Lett.*, 2015, **6**, 3263.

16 N. Feng, W. Mi, Y. Cheng, Z. Guo, U. Schwingenschlögl and H. Bai, *Sci. Rep.*, 2014, **4**, 3987.

17 J. Nian, Y. Si and Z. Guo, *Tribol. Int.*, 2016, **94**, 1.

18 G. Z. Ma, B. S. Xu, H. D. Wang and H. J. Si, *Mater. Rev.*, 2010, **24**, 1.

19 L. Hromadová, R. Martoňák and E. Tosatti, *Phys. Rev. B*, 2013, **87**, 144105.

20 A. Kumar and P. K. Ahluwalia, *Eur. Phys. J. B*, 2012, **85**, 186.

21 Q. H. Wang, K. Kalantar-Zadeh, A. Kis, J. N. Coleman and M. S. Strano, *Nat. Nanotechnol.*, 2012, **7**, 699.

22 H. R. Gutiérrez, N. Perea-López, A. L. Elías, A. Berkdemir, B. Wang, R. Lv, F. López-Urías, V. H. Crespi, H. Terrones and M. Terrones, *Nano Lett.*, 2013, **13**, 3447.

23 N. Perea-López, A. L. Elías, A. Berkdemir, A. Castro-Beltran, H. R. Gutiérrez, S. M. Feng, R. T. Lv, T. Hayashi, F. López-Urías, S. Ghosh, B. Muchharla, S. Talapatra, H. Terrones and M. Terrones, *Adv. Funct. Mater.*, 2013, **23**, 5511.

24 N. Perea-López, Z. Lin, N. R. Pradhan, A. Iñiguez-Rábago, A. L. Elías, A. McCreary, J. Lou, P. M. Ajayan, H. Terrones, L. Balicas and M. Terrones, *2D Mater.*, 2014, **1**, 011004.

25 M. Bernardi, M. Palummo and J. C. Grossman, *Nano Lett.*, 2013, **13**, 3664.

26 L. Britnell, R. M. Ríbeiro, A. Eckmann, R. Jalil, B. D. Belle, A. Mishchenko, Y. J. Kim, R. V. Gorbachev, T. Georgiou, S. V. Morozov, A. N. Grigorenko, A. K. Geim, C. Casiraghi, A. H. C. Neto and K. S. Novoselov, *Science*, 2013, **340**, 1311.

27 S. Wi, H. Kim, M. K. Chen, H. Nam, L. J. Guo, E. Meyhofer and X. G. Liang, *ACS Nano*, 2014, **8**, 5270.

28 M. Chhowalla, H. S. Shin, G. Eda, L.-J. Li, K. P. Loh and H. Zhang, *Nat. Chem.*, 2013, **5**, 263.

29 Z. Zeng, C. Tan, X. Huang, S. Bao and H. Zhang, *Energy Environ. Sci.*, 2014, **7**, 797.

30 J. K. Noerskov, T. Bligaard, A. Logadottir, J. R. Kitchin, J. G. Chen, S. Pandelov and U. Stimming, *J. Electrochem. Soc.*, 2005, **152**, J23.

31 T. F. Jaramillo, K. P. Joergensen, J. Bonde, J. H. Nielsen, S. Horch and I. Chorkendorff, *Science*, 2007, **317**, 100.

32 G. Levita, A. Cavaleiro, E. Molinari, T. Polcar and M. C. Righi, *J. Phys. Chem. C*, 2014, **118**, 13809.

33 G. Levita, E. Molinari, T. Polcar and M. C. Righi, *Phys. Rev. B*, 2015, **92**, 085434.

34 A. R. Lansdown, *Molybdenum Disulphide Lubrication*, Elsevier, Amsterdam, 1st edn., 1998.

35 J. M. Martin, H. Pascal, C. Donnet, Th. Le Mogne, J. L. Loubet and T. Epicier, *Surf. Coat. Technol.*, 1994, **68/69**, 427.

36 J. M. Martin, C. Donnet, Th. Le Mogne and T. Epicier, *Phys. Rev. B*, 1993, **48**, 48.

37 A. Blumberg, U. Keshet, I. Zaltsman and O. Hod, *J. Phys. Chem. Lett.*, 2012, **3**, 1936.

38 O. Hod, *Isr. J. Chem.*, 2010, **50**, 506.

39 O. Hod, *Chem. Phys. Chem.*, 2013, **14**, 2376.

40 T. Onodera, Y. Morita, R. Nagumo, R. Miura, A. Suzuki, H. Tsuboi, N. Hatakeyama, A. Endou, H. Takaba, F. Dassenoy, C. Minfray, L. Joly-Pottuz, M. Kubo, J.-M. Martin and A. Miyamoto, *J. Phys. Chem. B*, 2010, **114**, 15832.

41 O. Hod, *Phys. Rev. B*, 2012, **86**, 075444.

42 N. Marom, J. Bernstein, J. Garel, A. Tkatchenko, E. Joselevich, L. Kronik and O. Hod, *Phys. Rev. Lett.*, 2010, **105**, 046801.

43 A. Kolmogorov and V. Crespi, *Phys. Rev. B*, 2005, **71**, 235415.

44 A. N. Kolmogorov and V. H. Crespi, *Phys. Rev. Lett.*, 2000, **85**, 4727.

45 T. Liang, W. G. Sawyer, S. S. Perry, S. B. Sinnott and S. R. Phillpot, *Phys. Rev. B*, 2008, **77**, 104105.

46 Z. Wang, Q. Chen and J. Wang, *J. Phys. Chem. C*, 2015, **119**, 4752.

47 G. Kresse and J. Furthmüller, *J. Comput. Mater. Sci.*, 1996, **6**, 15.

48 G. Kresse and J. Hafner, *Phys. Rev. B*, 1993, **47**, 558.

49 G. Kresse and J. Hafner, *Phys. Rev. B*, 1993, **48**, 13115.

50 G. Kresse and J. Hafner, *Phys. Rev. B*, 1994, **49**, 4251.

51 P. E. Blöchl, *Phys. Rev. B*, 1994, **50**, 17953.

52 G. Kresse and D. Joubert, *Phys. Rev. B*, 1999, **59**, 1758.

53 J. P. Perdew, K. Burke and M. Ernzerhof, *Phys. Rev. Lett.*, 1996, **77**, 3865.

54 S. Grimme, *J. Comp. Chem.*, 2006, **27**, 1787.

55 A. Cammarata and T. Polcar, *Inorg. Chem.*, 2015, **54**, 5739.

56 H. J. Monkhorst and J. D. Pack, *Phys. Rev. B*, 1976, **13**, 5188.

57 *ISOTROPY Software Suite*, `http://iso.byu.edu/iso/isotropy.php`.

58 H. T. Stokes and D. M. Hatch, *J. Appl. Cryst.*, 2005, **38**, 237.

59 *OSU Http Server on the Applied Crystallography Group DEC Alpha Homepage*, `http://img.chem.ucl.ac.uk/sgp/large/sgp.htm`.

60 *CDS/DL Homepage*, `http://cds.dl.ac.uk/`.

61 A. M. Homola, J. N. Israelachvili, M. L. Gee and P. M. McGuiggan, *J. Tribol.*, 1989, **111**, 675.

62 R. W. Carpick, N. Agraït, D. F. Ogletree and M. Salmeron, *J. Vac. Sci. Technol. B*, 1996, **14**, 1289.

63 R. W. Carpick, N. Agraït, D. F. Ogletree and M. Salmeron, *Langmuir*, 1996, **12**, 3334.

64 M. Xia, B. Li, K. Yin, G. Capellini, G. Niu, Y. Gong, W. Zhou, P. M. Ajayan and Y.-H. Xie, *ACS Nano*, 2005, **9**, 12246.

65 M. J. Sutcliffe, S. R. Taylor and A. Cameron, *Wear*, 1978, **51**, 181.

66 G. M. McLelland, *Adhesion and Friction*, Springer Series in Surface Sciences, New York, 1989, vol. 17.

67 A. M. Homola, J. N. Israelachvili, P. M. McGuiggan and M. L. Gee, *Wear*, 1990, **136**, 65.

68 A. L. Allred, *J. Inorg. Nucl. Chem.*, 1961, **17**, 215.

69 L. Pauling, *The Nature of the Chemical Bond*, Cornell University, USA, 3rd edn., 1961.

70 Y. Guo and J. Robertson, *Appl. Phys. Lett.*, 2016, **108**, 233104.

71 A. Yan, J. Velasco Jr., S. Kahn, K. Watanabe, T. Taniguchi, F. Wang, M. F. Crommie and A. Zettl, *Nano Lett.*, 2015, **15**, 6324.

72 N. T. Nguyen, P. A. Berseth, Q. Lin, C. Chiritescu, D. G. Cahill, A. Mavrokefalos, L. Shi, P. Zschack, M. D. Anderson, I. M. Anderson and D. C. Johnson, *Chem. Mater.*, 2010, **22**, 2750.

73 B. Ivković, M. Djurdjanović and D. Stamenković, *Tribol. Ind.*, 2000, **22**, 41.

74 T. F. T. Cerqueira, R. Sarmiento-Pérez, M. Amsler, F. Nogueira, S. Botti and M. A. L. Marques, *J. Chem. Theory Comput.*, 2015, **11**, 3955.

75 K. Momma and F. Izumi, *J. Appl. Crystallogr.*, 2011, **44**, 1272.